Ferromagnetic micromechanical magnetometer

H.H. Yang[a,*], N.V. Myung[b], J. Yee[a], D.-Y. Park[b], B.-Y. Yoo[b],
M. Schwartz[b], K. Nobe[b], J.W. Judy[a]

[a]*Department of Electrical Engineering, University of California at Los Angeles, 420 Westwood Plaza, Los Angeles, CA 90095-1594, USA*
[b]*Department of Chemical Engineering, University of California at Los Angeles, 420 Westwood Plaza, Los Angeles, CA 90095-1594, USA*

Abstract

A novel micromechanical magnetometer has been designed, fabricated, and tested that consists of low-stress electrodeposited magnetic alloys and surface-micromachined polysilicon structures. The sensor responds to applied magnetic fields without consuming any power and the magnitude of the angular response is scale independent. Theoretical models are developed and their predictions agree well with experimental results. Mechanical responses to fields as small as 200 nT have been optically detected for a micromechanical magnetometer with a $1000\,\mu m^3 \times 100\,\mu m^3 \times 10\,\mu m^3$ 60Ni40Co magnetic element and a pair of $100\,\mu m^3 \times 4\,\mu m^3 \times 2\,\mu m^3$ polysilicon torsion beams.
© 2002 Elsevier Science B.V. All rights reserved.

Keywords: MEMS magnetometer; Ferromagnetic materials; Electrodeposition

1. Introduction

Magnetometers have very practical applications such as compassing, ferrous object or magnetic anomaly detection, and mineral prospecting. In these applications smaller, lower power, and cheaper magnetometers would be advantageous. Microelectromechanical systems (MEMS) technology can be used to reduce the size of many types of sensors as well as increase their ability to be mass produced (e.g. pressure sensors and accelerometers). A small magnetometer with low power consumption would also be useful for wireless microsensor networks, which have commercial and military applications, such as perimeter security, shoreline reconnaissance, and personnel or asset monitoring [1]. From a surveillance application standpoint, small magnetometers would be harder to detect and easily deployed.

Miniaturization of magnetometers using MEMS technology has been reported in several studies [2–5]. Wickenden et al. fabricated a polysilicon xylophone-bar magnetometer with a sensitivity of order 100 nT [2]. Wandass et al. proposed a magnetic field sensor using a tunneling tip [3] and achieved a sensitivity of 2000 nT. More recently DiLella et al. reported a similar MEMS tunneling magnetometer [4]. Instead of using the wire loop of Wandass's study, DiLella et al. used a glued-on neodymium iron–boron magnet as the

sensing element to achieve a sensitivity of $0.002\,nT/\sqrt{Hz}$. The device, being nearly 1 cm², is relatively large for MEMS, and its fabrication requires microassembly to glue on the magnetic material. Latorre et al. reported a torsional ferromagnetic magnetometer integrated with CMOS and employing a piezoresistive strain gauge for the sensor output [5].

We propose a novel method of fabricating micromechanical magnetometers using polysilicon mechanical flexures and electrodeposited ferromagnetic alloys as the sensing element. In these prototype devices the mechanical response is measured optically and a sensitivity of 200 nT has been achieved.

2. Theory

2.1. Mechanical theory

The compass is the earliest known magnetometer, placed by historians in China between 2637 BC and 1100 AD [6]. In a typical compass, a ferromagnetic needle with magnetization $\vec{M}$ and volume V_{mag} is mechanically driven to align the magnetization with the external field $\vec{H}$. The torque experienced by the magnet $\vec{T}_{mag}$ is given by

$$\vec{T}_{mag} = (\vec{M} \times \vec{H})V_{mag}. \tag{1}$$

Essentially, we propose mounting the magnet onto a micromachined polysilicon plate that is bisected by torsion beams.

* Corresponding author. Tel.: +1-310-794-5774; fax: +1-877-349-3134.
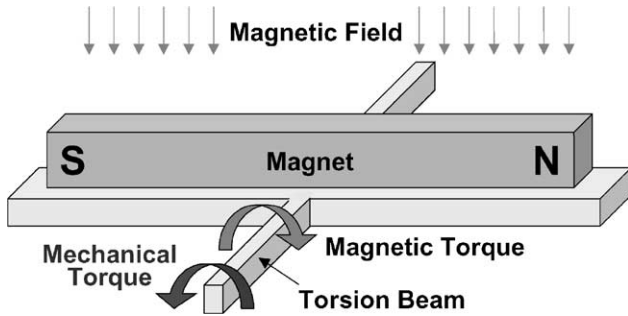*E-mail address:* hry@ee.ucla.edu (H.H. Yang).

Fig. 1. Schematic representation of micromechanical magnetometer operation.

Fig. 1 illustrates a schematic representation of our magnetometer design. When the magnet is mechanically deflected, the torsion beam applies a mechanical restoring torque $\vec{T}_{\text{mech}}$, which is defined as

$$\vec{T}_{\text{mech}} = k_\phi \phi, \tag{2}$$

with torsional beam stiffness k_ϕ and angular deflection $\vec{\phi}$. A detailed analysis can be found in [7].

When the magnet is placed in a field, the equilibrium established between the magnetic and the mechanical torque (i.e. $\vec{T}_{\text{mag}} = \vec{T}_{\text{mech}}$) determines the resultant angular deflection of the magnet. Equating the two torques given by (1) and (2) and solving for the angle of rotation $\vec{\phi}$ yields:

$$\vec{\phi} = \frac{(\vec{M} \times \vec{H}) V_{\text{mag}}}{k_\phi}. \tag{3}$$

Although V_{mag} scales with the volume of the magnet, k_ϕ also has a cubic dimensional dependence. Thus, the angle of rotation $\vec{\phi}$ is independent of the scale of the device. As an example, a magnetometer with a $1000\,\mu\text{m}^3 \times 100\,\mu\text{m}^3 \times 10\,\mu\text{m}^3$ magnet, a pair of $100\,\mu\text{m}^3 \times 4\,\mu\text{m}^3 \times 2\,\mu\text{m}^3$ torsion beams, and a magnetization $\vec{M}$ of 1.0 nT, in a field of 200 nT would have an angular deflection of 15.76 µrad and a tip deflection of 8 nm, which could be detected with optical or capacitive techniques.

2.2. Magnetic theory

The magnetization of ferromagnetic material has a hysteretic dependence on magnetic field. When the field is increased and then brought back to zero, the material has a non-zero remanent magnetization $\vec{M}_{\text{r}}$. Ferromagnetic materials can be classified into soft and hard magnetic materials and magnets can have easy and hard magnetic axis. A soft magnetic material is easily magnetized (i.e. typically it has a low coercivity $\vec{H}_{\text{c}}$) whereas a hard magnetic material has a higher coercivity and saturating field $\vec{H}_{\text{s}}$. Fig. 2 illustrates a comparison between a soft and hard magnetic material. Coercivity is a structure-sensitive property that depends on crystal structure, grain size, preferred orientation, stress, defect density, thickness, among other effects. The saturating field is dependent on the microstructure of the film as well as the overall shape of magnetic element.
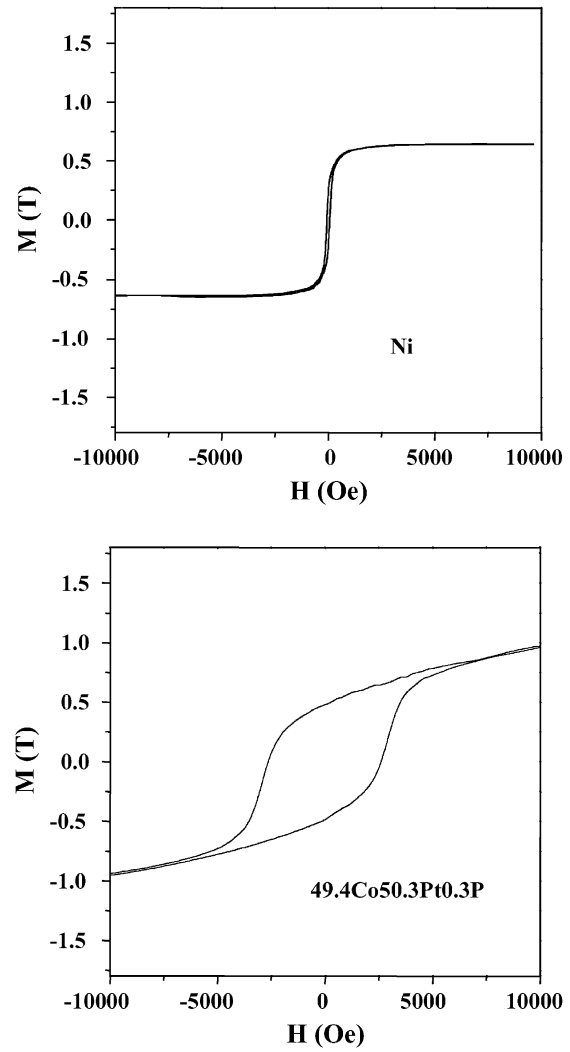

Fig. 2. A comparison between the hysteresis loops of magnetically soft (Ni) and hard (49.4Co50.3Pt.3P) materials.

A simple bar magnet containing two poles will create the well-known field outside of the magnet as well as a lesser-known field inside the magnet. The magnetization of the ferromagnetic element is written as a vector $\vec{M}$ directed from the south pole to the north pole. The magnetic field generated by the poles is represented by a vector $\vec{H}$ directed from the north pole to the south pole, both outside and inside the material. The field outside the magnet is easily observed. The portion of the magnetic field generated by the poles that lies within the magnet is called the demagnetizing field $\vec{H}_{\text{d}}$, as it is directed in opposition to the magnetization $\vec{M}$. The demagnetizing field is directly proportional to $\vec{M}$ and is given by

$$\vec{H}_{\text{d}} = N_{\text{d}} \frac{\vec{M}}{\mu_0}, \tag{4}$$

with permeability of free space μ_0 and shape dependent coefficient N_{d}. In order to determine the shape dependence of the demagnetizing field it is helpful to consider an
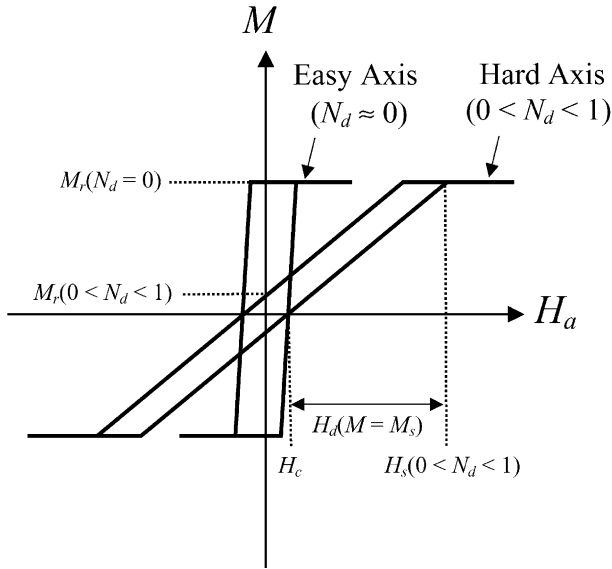
Fig. 3. Hysteresis loops of an idealized ferromagnetic material along its magnetically easy ($N_d \approx 0$) and hard ($0 < N_d < 1$) axis.

electrostatic analogue. Given that the poles on the end of a magnet can be modeled as a charge density on the plates of a capacitor, the demagnetizing field is analogous to the electric field inside the capacitor. When the capacitor plates have small area and are far apart, the internal electric field is small and such a magnet would have a low demagnetizing field. When the plates are larger and closer together, the internal field and corresponding demagnetizing field would be large.

When magnetizing a magnet, the applied field $\vec{H}_a$ is opposed by the demagnetizing field $\vec{H}_d$ and the resulting net internal magnetic field is $\vec{H}_i = \vec{H}_a - \vec{H}_d$. The internal field $\vec{H}_i$ is responsible for determining the level of magnetization as defined by the $\vec{B} - \vec{H}$ loop of the material when

the demagnetizing field is approximately zero (Fig. 3, $N_d = 0$). When the material is used in a situation where the demagnetizing field is not zero, the resulting remanent magnetization is reduced considerably (Fig. 3, $0 < N_d < 1$). It is for these reasons that an element of ferromagnetic material is more easily magnetized along its long axis (i.e. easy magnetic axis) than along its short axis (i.e. hard magnetic axis).

3. Fabrication

The fabrication of the device is divided into four parts: structure fabrication, seed layer patterning, electrodeposition, and release.

3.1. Structure fabrication

The MUMPs® prototyping foundry service from JDS Uniphase MEMS Business Unit is used to fabricate the polysilicon microstructures [8]. Polysilicon structural layers used to construct the magnetometers are poly1 (2 µm thick) and poly2 (1.5 µm thick). Dimples and etch holes are added to minimize stiction and release etch time. Design variations include magnetic plate length and torsion beam stiffness. A total of 251 devices are fabricated per 1 cm² die. Fig. 4 shows a few design variations that have been fabricated. Both single and double-ended devices are fabricated although only double-ended devices are considered in this study.

3.2. Seed layer patterning

In our previous report [9], the fabrication consisted of the following steps: (1) cleaning the MUMPs die with a resist
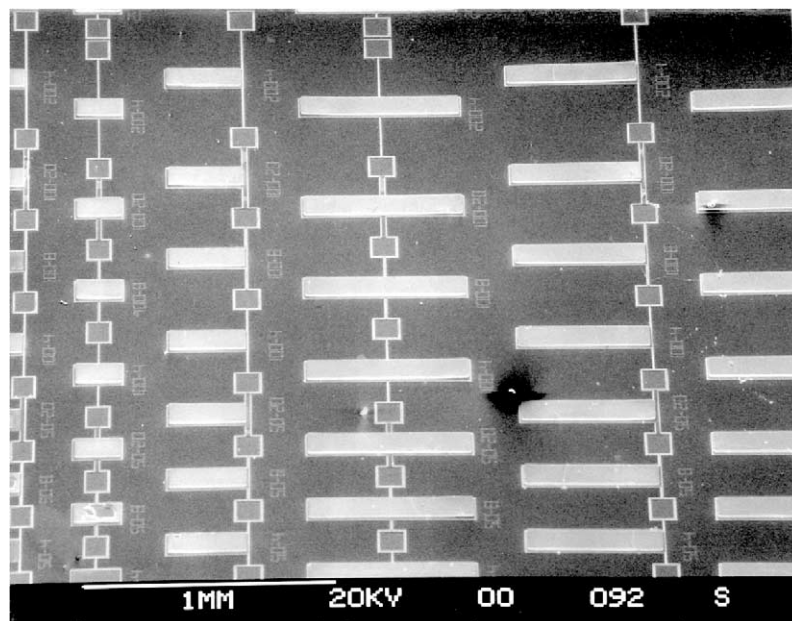

Fig. 4. Design variations fabricated with the MUMPs prototyping service.

stripper (Mallinckrodt Baker Inc. Aleg 310) to remove photoresist and organic residue from the surface, (2) etching the oxide from the surface of the polysilicon microstructures in a timed 10:1 HF etch (3 min 47 s), (3) depositing an e-beam evaporated (CHA Mark 40) seed layer consisting of chromium (10 nm) and nickel (20 nm) onto the entire chip, (4) patterning a 10 μm thick photoresist layer (Shipley SJR5740) to form a plating mold into which a hard magnetic material is electrodeposited (note: Shipley SJR5740 was selected for its good chemical stability, a crucial characteristic when electrodepositing in highly acidic solutions that could otherwise quickly compromise photoresist integrity), (5) stripping the resist in Mallinckrodt Baker Inc. Aleg 310 after electrodeposition, (6) selectively removing the seed layer, and (7) releasing the device by etching away the sacrificial oxide (49% HF for 4 min).

Unfortunately, the removal of the seed layer using wet chemical etchants (i.e. step 6 as described above) became a significant challenge. When removing the nickel seed layer with a commercial nickel etchant (Transene Nickel Etchant TFB) galvanic coupling effect between the seed layer (Cr/Ni) and the electrodeposited layer (85Co15Ni) made it energetically favorable to etch the electrodeposited layer. In fact, the much thicker electrodeposited magnet (10 μm) was completely removed before the e-beam evaporated seed layer of 20 nm Ni and 10 nm Cr was removed. The 85Co15Ni alloy is preferentially oxidized by the etchant while the chromium adhesion layer acted as reducing site. This effect was not observed when removing a Cr/Ni seed layer around an electrodeposited Ni magnet.

Sputter etching (CVC sputtering system) was used to work around the problem, since it is a purely physical etch (i.e. there is no galvanic reaction). In addition, both chromium and nickel can be removed in the same step. Although the sputter etch was effective in removing the seed layer, the temperature of the chip during the etch was relatively high (>260 °C). A significant thermal expansion mismatch between the polysilicon and the electrodeposited magnetic material, resulted in a catastrophic structural deformation (e.g. structures consisting of poly1 and deposited magnetic material were forcibly delaminated from the oxide1 layer underneath). The tip of 500 μm long cantilever beams, consisting of electrodeposited material and polysilicon, curled to a vertical deflection of ∼18 μm. Even though the fabrication method was not ideal and the yield was low, functional devices were fabricated and experimental results that matched expectations were obtained [9]. Finding a way to remove the seed layer without sputter etching was critical to increase yield. Furthermore, the curvature resulting from the sputter etching process could strongly impact the performance of the capacitive sensing scheme planned for future integration. In addition, when ICs are integrated with the micromechanical magnetometer, sputter etching could result in plasma induced circuit damage.

The solution used in this work is to pattern two types of seed layer. One seed layer has good adhesion, high release

etch resistance, and is patterned to form islands used as the electrodeposition base for the electrodeposited magnet. The second seed layer, named the conduction layer, is deposited over the entire chip and is used to electrically connect the islands of the first seed layer. The primary characteristic of the second layer is that it is conductive and can be selectively etched without attacking the electrodeposited magnet.

A three-mask post-foundry process was developed. The first mask uses lift-off to define the regions where 10 nm of chromium and 100 nm of nickel are deposited by e-beam evaporation. It is on these Cr/Ni islands that thick magnetic material will be electrodeposited. Again using lift-off, the second mask defines the areas where 10 nm of titanium and 100 nm of copper are deposited by e-beam evaporation. The titanium under the copper improves adhesion to the oxide, and the titanium on top improves the adhesion of photoresist. The masks are designed such that the Cr/Ni and Ti/Cu/Ti films have a 5 μm wide overlap. This overlap insures the electrical connectivity necessary for electrodeposition and avoids stringers (i.e. sidewall structures remaining after an anisotropic etch). Finally, the 15 μm thick electrodeposition mold is patterned using SJR5740 resist. See Fig. 5 for a cross-section of the processes. Although this method yielded a high fidelity electrodeposition, we were unable to develop a copper etchant with high selectivity. The 10 μm thick electrodeposited 60Co40Ni was etched down to 3 μm by the time the 100 nm thick copper film was completely etched in a mixture of 1:1:10 acetic acid, peroxide, and DI water. Clearly, an even more selective method was needed.

Although titanium has a resistivity 25 times higher than copper [10], it can be rapidly and selectively removed by dilute HF. The electrodeposition system regulates the current, so the increased resistivity only results in a higher potential and does not change the current density. Using titanium as the conduction layer also reduced the number of masks needed from three to two. After the patterning of the Cr/Ni seed layer as described above, 100 nm of titanium is deposited everywhere using e-beam evaporation. Immediately after titanium deposition, the electrodeposition mold is patterned. Prior to electrodeposition, a 2 min 200:1 HF etch selectively removes the titanium from the areas unprotected by the electrodeposition mold. In addition to a simplification in the process, this method also results in no significant
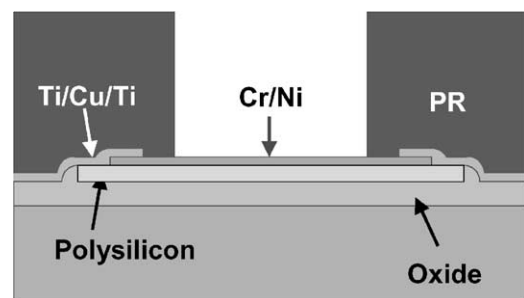

Fig. 5. Cross-section of the fabrication process that uses a copper conduction layer.
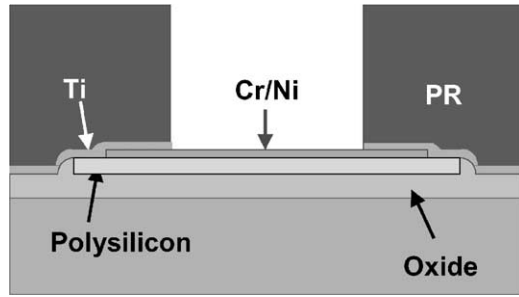
Fig. 6. Cross-section of the fabrication process that uses titanium conduction layer.

etching of the electrodeposited magnet. The process cross-section can be found in Fig. 6.

3.3. Electrodeposition

Electrodeposition has many advantages over other deposition techniques for the microfabrication of IC-compatible hard magnetic materials. The magnetic properties of the films can be tailored for specific applications, since they are strongly influenced by electrodeposition parameters (e.g. solution composition, pH, current density, temperature, agitation, and current waveform). Various hard magnetic materials have been electrodeposited to evaluate the relationships between electrodeposition parameters, microstructure, and magnetic properties (Table 1) [11]. In addition, the compatibility of electrodeposited hard magnetic materials with other MEMS processes has been studied.

To integrate electrodeposited magnetic materials with ICs and MEMS, the electrodeposited materials must have: (1) low deposit stress to prevent film cracking and structure deformation, (2) good adhesion between the seed layer and the electrodeposited films, and (3) corrosion resistance to HF and other acids that are frequently employed in MEMS fabrication. In order to reduce the stress of electrodeposits, various electrodeposition parameters, including solution composition (e.g. additives and anions) and deposition temperature, must be investigated. The most effective factor to control the stress of electrodeposited thin films is additives (e.g. saccharin). Fig. 7 illustrates the dependence of
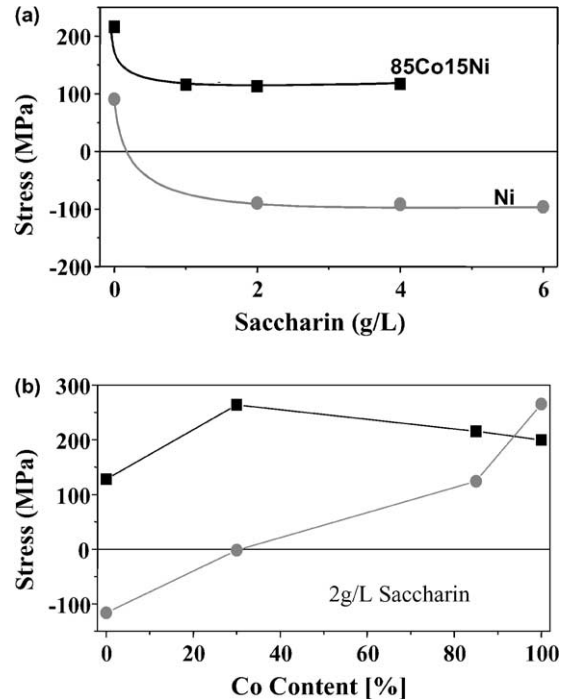

Fig. 7. The dependence of film stress on (a) saccharin concentration and (b) cobalt content (saccharin concentration kept at 2 g/l).

film stress on saccharin concentration and Co content in electrodeposited CoNi films. Film stress sharply decreased initially then reached a plateau with increasing saccharin concentration (i.e. from 100 to −100 MPa for Ni and from 216 to 115 MPa for 85Co15Ni films.

Adhesion between electrodeposited hard magnetic materials and the nickel seed layer has been improved by activating the nickel surface with 20% HCl for 1 min and briefly electrodepositing nickel in a Ni "strike" solution (1 M $NiCl_2$ + 4% v/v HCl, current densities 25–50 mA/cm^2) before plating the thick magnet.

Presently, 40Co60Ni is deposited for its low-stress and high corrosion resistance. Although the device performs well using this alloy, its properties are inferior to other hard magnetic materials we have developed (Table 1). We hope to develop a method to protect corrosion sensitive alloys so that the release etch will not limit material selection.

Table 1
Magnetic properties of electrodeposited alloys

Plated alloys	Composition (wt.%)	Coercivity (Oe) (thickness)	M_s (T)	Squareness[a]
Ni	100	50 (∥) (2 μm)	0.6	0.25 (∥)
CoNi	60 Ni	35–50 (∥) (2 μm)	1.0	0.3 (∥)
CoNi	15 Ni	75 (∥), (2 μm)	1.6	0.8 (∥)
CoP	2–4 P	1400 (∥), 1300 (⊥), (2 μm)	1.5–1.6	0.2–0.5 (∥), 0.1–0.3 (⊥)
CoPt	30–58 Pt	1653 (∥), 2102 (⊥) (1 μm)	1.2–0.7	0.34–0.64 (∥), 0.25–0.07 (⊥)
CoNiP	18–37 Ni, 1–3 P	926 (∥), 2150 (⊥), (2 μm)	1.2–1.4	0.2–0.45 (∥), 0.1–0.3 (⊥)
CoMnP	2–4 P, <1 Mn	800 (∥), 2000 (⊥), (2 μm)	1.4–1.5	0.1–0.3 (∥), 0.1–0.2 (⊥)
CoPtP	58 Pt 1P	2887 (∥), 3555 (⊥), (1 μm)	0.7	0.4–0.6 (∥), 0.3–0.4 (⊥)
Co₃W/CoW	30–40 W	250 (∥), (2 μm)	1.2–1.3	0.2–0.5 (∥)

[a] Squareness = M_r/M_s.

3.4. Release

Once the chip is electrodeposited, the resist is stripped at 80 °C. To avoid thermal shock, the chip is placed in a water bath and ramp heated with the resist stripper upto 80 °C. Once 80 °C is reached, the chip is moved from the water bath to the stripper bath. At the completion of the resist strip, the chip is placed back in the heated water bath and cooled by dilution with room-temperature water. After resist striping, the titanium conduction layer is etched using 200:1 HF. Once the titanium is completely removed, the chip is placed in 49% HF for 4 min to release the microstructures. The chip is then dried using a CO_2 supercritical dryer (Polaron E3000).

3.5. Fabrication results

The fabrication yield with the improved process is extremely high (i.e. 250 out of 251 devices survived fabrication). Magnetic material is deposited into electrodeposition molds that have a smooth and vertical sidewall profile and a 2:1 height-to-width aspect ratio. Pillars of photoresist are
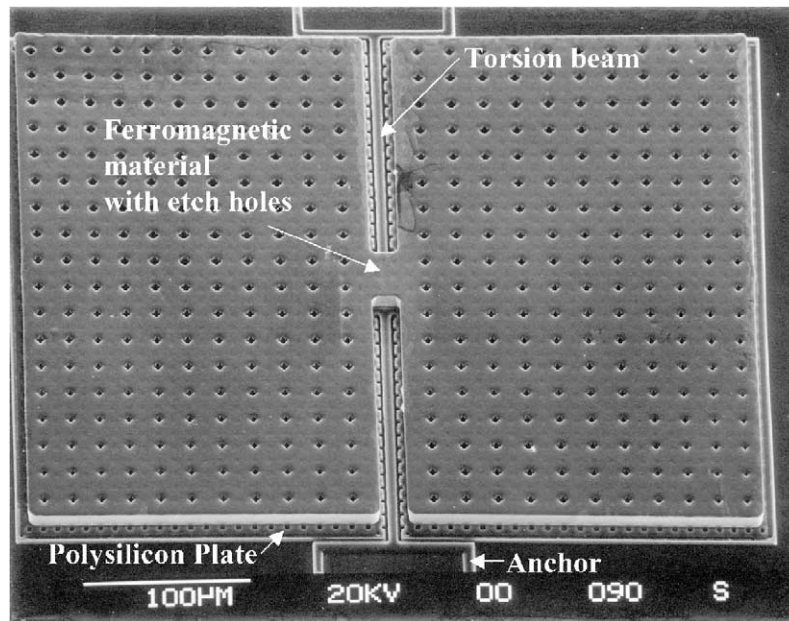

Fig. 8. SEM image of a patterned electrodeposited ferromagnetic material on a polysilicon structure.
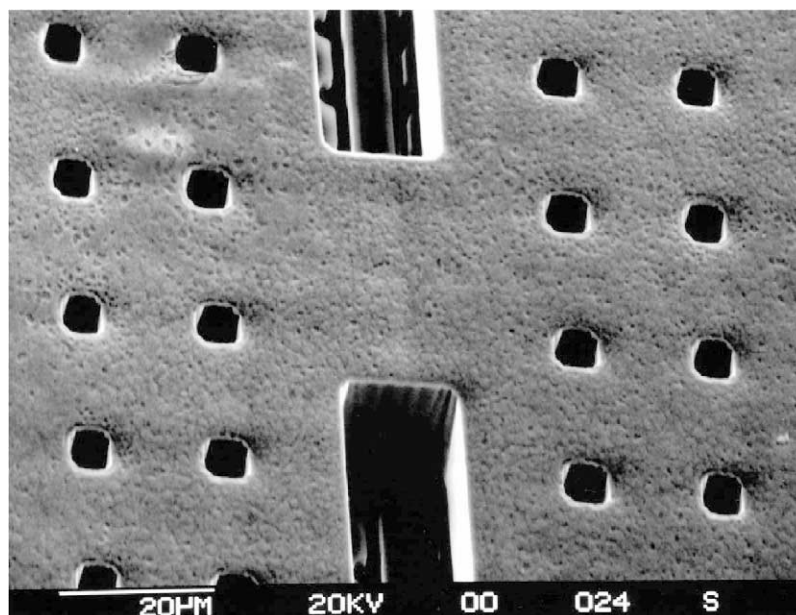

Fig. 9. Close-up SEM image of a patterned electrodeposited ferromagnetic material.
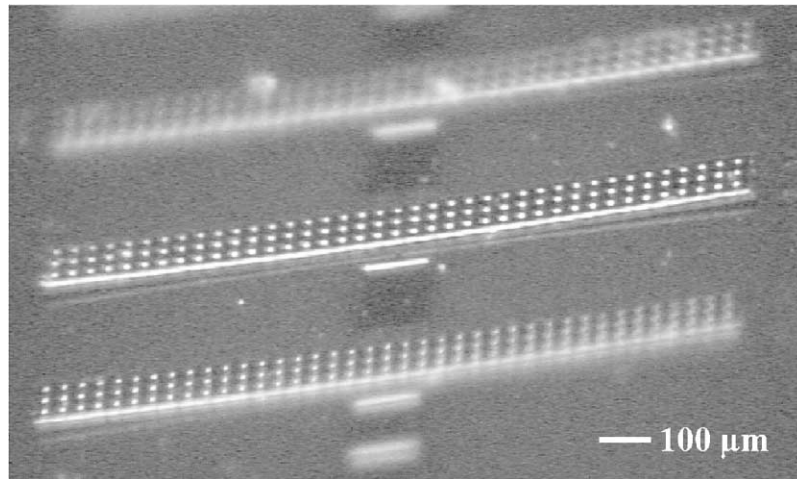
Fig. 10. Stereo microscope image of a released magnetometer with the following dimensions; $1000\,\mu m^3 \times 100\,\mu m^3 \times 10\,\mu m^3$ magnetic plate and $50\,\mu m^3 \times 8\,\mu m^3 \times 2\,\mu m^3$ torsion beams.

positioned on the etch holes to prevent the electrodeposited material from blocking the etch holes. Fig. 8 shows a magnetometer with patterned ferromagnetic material and etch holes. Fig. 8 shows a closer view of the sidewall profile.

During release etch in 49% HF, no failure due to chemical etching was observed. In addition, stiction was not an issue even for $1000\,\mu m^2 \times 100\,\mu m^2$ devices as long as $1000\,\mu m$. Figs. 9 and 10 shows a stereo microscope image of a released magnetometer with a $1000\,\mu m^3 \times 100\,\mu m^3 \times 10\,\mu m^3$ ferromagnetic plate. Notice that although we attempted to minimize the stress of the deposited material, the magnetometer is still slightly deformed.

4. Magnetic testing setup

After release, the devices are tested in an ac magnetic field (0.5–1000 Hz) generated by a 111-turn 1.7 cm diameter coil.

The field generated is applied perpendicularly to the permanent magnet of the magnetometer. A laser Doppler vibrometer (Polytec OFV 511) is used to measure the tip displacement of the magnetometer. A lock-in amplifier (Stanford Research Systems SR 850) is used to improve the signal-to-noise ratio.

5. Results

To verify that devices are rotating about the torsional axis, the deflection of a device is measured along the entire length of the magnet. If the device is working properly, the deflection should be a maximum at the ends of the magnet and decreases linearly as the measurement approaches the torsional axis. Fig. 11 indicates a properly working device.

As previously mentioned, the magnetization is a function of shape. Given that we know the geometry, magnetic field
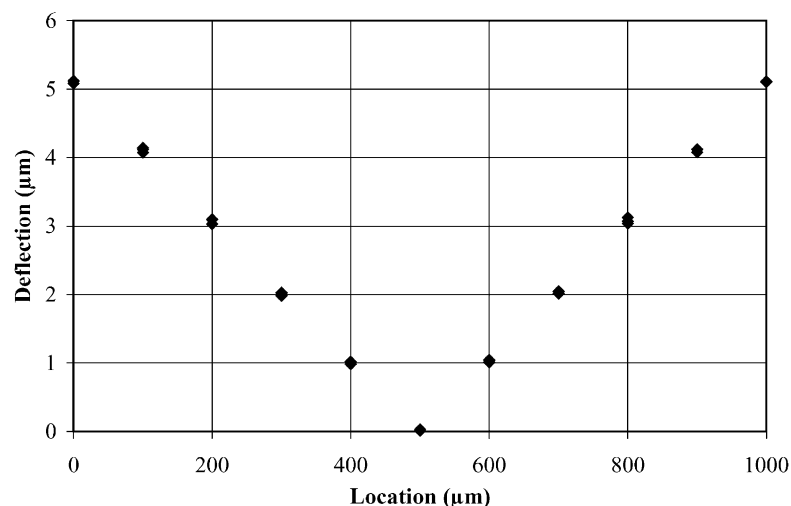

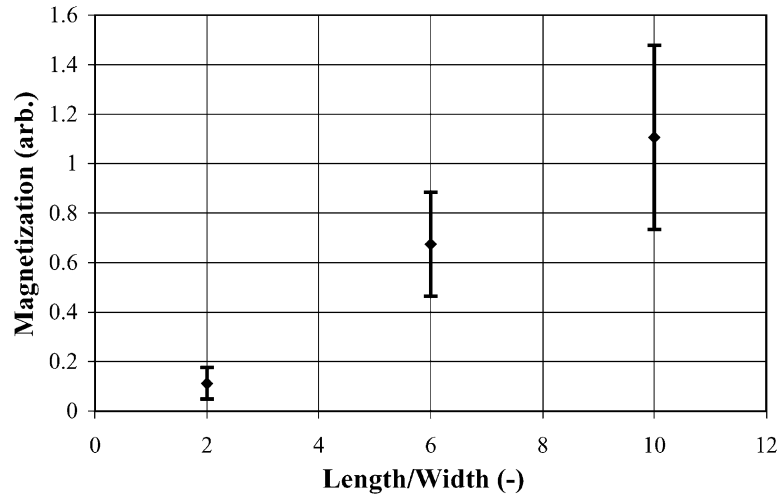Fig. 11. Deflection along the length of a 1000 μm long magnetometer.

Fig. 12. Magnetization increases with length-to-width ratio, due to the decreasing demagnetization field.

direction, field magnitude, and angular deflection, the magnetization of the devices can be determined by equating Eqs. (1) and (2) and solving for magnetization. Fig. 12 shows magnetization as a function of magnetometer length-to-width ratio. As expected, increasing the length-to-width ratio will decrease the demagnetization field, thereby increasing the remanent magnetization $\vec{M}_r$. A higher remanent magnetization will result in a larger angular deflection and a more sensitive device.

Fig. 13 shows the performance of three magnetometers with different magnetic plate geometries and the same torsion beam stiffness. As the plate length decreases, the remanent magnetization and volume also decreases, with the result being a less sensitive device.

For magnetometers with the same magnetic plate dimensions, altering the torsion beam stiffness can also impact performance as shown in Fig. 14. The most compliant beam results in the most sensitive device.

We have also designed devices with and without etch holes to investigate their effect on magnetometer performance. Fig. 15 shows the performance of two magnetometers, one
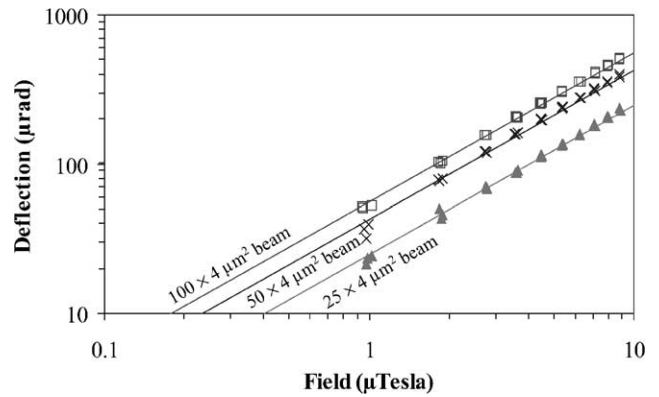

Fig. 14. Magnetometer performance as function of beam stiffness for magnetic plate width 100 μm and length 1000 μm.

with etch holes and one without. The magnetometer with etch holes performs slightly better than the one without. Although the volume of the magnetic material is reduced by the use of etch holes, the remanent magnetization can be increased due to the higher coercivity induced by the increased defect
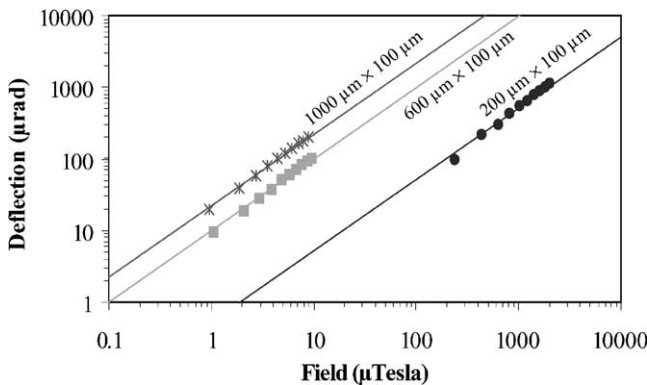

Fig. 13. Performance of magnetometers with $100 \, \mu m^3 \times 8 \, \mu m^3 \times 2 \, \mu m^3$ torsion beams and varying magnetic plate length (200, 600, and 1000 μm).
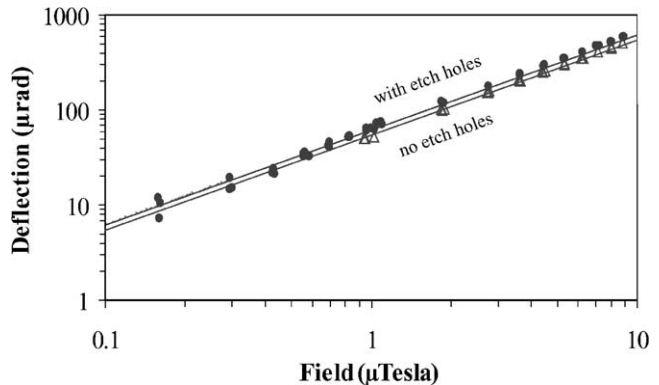

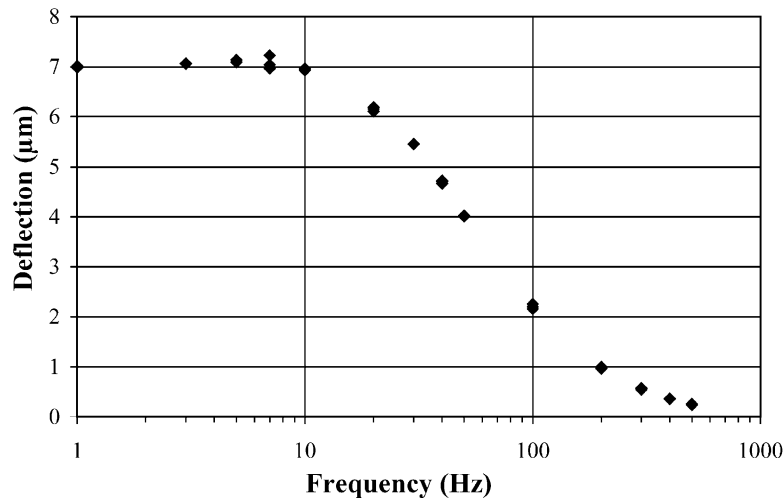Fig. 15. Effect of etch holes on magnetometer performance for two $1000 \, \mu m^2 \times 100 \, \mu m^2$ devices.

Fig. 16. Frequency response of a magnetometer with a $1000\,\mu m^3 \times 100\,\mu m^3 \times 10\,\mu m^3$ magnetic plate dimensions and $100\,\mu m^3 \times 4\,\mu m^3 \times 2\,\mu m^3$ torsion beams.

density that the etch holes provide [12]. We are able to detect a 200 nT ac field using the magnetometer with etch holes.

The frequency response of the device slightly peaks at 8 Hz, and then rolls with a 3 dB frequency of 62 Hz. The frequency response of a typical device is presented in Fig. 16. Although the device has a calculated natural frequency of 1 kHz, it is suspected that squeeze-film damping is the cause for the reduction of the roll-off frequency [13].

6. Future work

Although devices constructed with 40Co60Ni performed well, better materials should be implemented to achieve a higher remanent magnetization and performance. Since some better magnetic alloys may be attacked by HF, methods to improve their corrosion resistance are needed. One possible approach is to coat the magnetic material with a corrosion resistant layer. The squeeze-film damping phenomenon encountered is being correlated with existing models. Testing at different pressures would give us better understanding of this behavior. Magnetometers with integrated capacitive position sensing and piezoresistive strain measurement are also being developed.

7. Conclusion

A ferromagnetic micromechanical magnetometer based on the simple compass is predicted by theory to be scale independent. Sub-mm devices are predicted to be capable of detecting fields significantly smaller than 1 μT using optical or capacitive displacement measurement techniques. The microscale magnets can be integrated with the micromechanical structures by electrodeposition. The use of a two-step seed layer process avoids undesirable galvanic etching

that can occur during seed layer removal. Doing so results in a high-yield of functional devices (>90%). A device with $1000\,\mu m^3 \times 100\,\mu m^3 \times 10\,\mu m^3$ magnet and $100\,\mu m^3 \times 4\,\mu m^3 \times 2\,\mu m^3$ torsion beams has been used to detect fields as small as 200 nT. Theoretical models agree well with experimental results. Magnetometer performance can be improved by using materials and geometries that yield a higher remanent magnetization as well as integrated circuits to measure deflection with a higher resolution.

References

[1] K. Bult, A. Burstein, D. Chang, M. Dong, M. Fielding, E. Kruglick, J. Ho, F. Lin, T.H. Lin, W.J. Kaiser, H. Marcy, R. Mukai, P. Nelson, F.L. Newburg, K.S.J. Pister, G. Pottie, H. Sanchez, K. Sohrabi, O.M. Stafsudd, K.B. Tan, G. Yung, S. Xue, J. Yao, Low power systems for wireless microsensors, in: Proceedings of the 1996 International Symposium on Low Power Electronics and Design, Monterey, CA, 12–14 August 1996, pp. 17–21.

[2] D.K. Wickenden, J.L. Champion, R.B. Givens, T.J. Kistenmacher, J.L. Lamb, R. Osiander, Polysilicon xylophone-bar magnetometers, in: Technical Digest Solid-State Sensor and Actuator Workshop (Hilton Head 2000), Hilton Head Island, SC, 4–8 June 2000, pp. 150–153.

[3] J.H. Wandass, J.S. Murday, R.J. Colton, Magnetic field sensing with magnetostrictive materials using a tunnelling tip detector, Sens. Actuators A (Physical) 19 (3) (1989) 211–225.

[4] D. DiLella, L.J. Whitman, R.J. Colton, T.W. Kenny, W.J. Kaiser, E.C. Vote, J.A. Podosek, L.M. Miller, A micromachined magnetic-field sensor based on an electron tunnelling displacement transducer, Sens. Actuators A (Physical) A86 (1/2) (2000) 8–20.

[5] L. Latorre, V. Beroulle, Y. Bertrand, P. Nouet, I. Salesse, Micromachined CMOS magnetic field sensor with ferromagnetic actuation, in: Conference Proceedings on the Design, Test, Integration, and Packaging of MEMS/MOEMS, SPIE, Paris, France, 2000, pp. 398–405.

[6] D. Mattis. The Theory of Magnetism, Harper and Row, New York, 1965.

[7] J.W. Judy, R.S. Muller, H.H. Zappe, Magnetic microactuation of polysilicon flexure structures, J. Microelectromech. Syst. 4 (4) (1995) 162–169.

[8] JDS Uniphase MEMS Business Unit, www.memsrus.com.

[9] J.W. Judy, H.H. Yang, N.V. Myung, P. Irazoqui-Pastor, M. Schwartz, K. Nobe, K. Yang, Ferromagnetic micromechanical magnetometers, in: Proceedings of the Late News Update of Technical Digest Solid-State Sensor and Actuator Workshop (Hilton Head 2000), Hilton Head Island, SC, 4–8 June 2000, pp. 15–16.

[10] CRC Handbook of Chemistry and Physics, 1982–1983 edition, CRC Press, Boca Raton, FL, 1984.

[11] N.V. Myung, D.-Y. Park, M. Schwartz, K. Nobe, H.H. Yang, C.-K. Yang, J.W. Judy, Electrodeposited hard magnetic thin films for MEMS application, in: Proceedings of the Electrochemical Society PV2000-29, 2000.

[12] X. Fang, N.V. Myung, K. Nobe, J.W. Judy, Modeling the effect of etch holes on ferromagnetic MEMS, in: Conference Proceeding of the 8th Joint MMM-Intermag Conference 2001, San Antonio, TX, 2001, pp. 455–456.

[13] Y. Yang, M. Gretillat, S. Senturia, Effect of air damping on the dynamics of non-uniform deformations of microstructures, in: Proceedings of the Technical Digest 1997 International Conference on Solid-State Sensors and Actuators (Transducers'97), Chicago, IL, 16–19 June, 1997, pp. 1093–1096.

Biographies

Henry H. Yang received his BS degree in mechanical engineering from the University of California, Los Angeles, in 1999. He is currently finishing his MS degree in electrical engineering from the University of California, Los Angeles. He is also working as a staff engineer with the IBM Almaden Research Center in San Jose, CA. His present research includes magnetic MEMS and MEMS applications in data storage. He is a member of Tau Beta Pi.

Nosang V. Myung received his BS, MS, and PhD (1998) degree in chemical engineering from the University of California, Los Angeles. He is presently working as a staff engineer in the MEMS Group at NASA Jet Propulsion Laboratory (JPL), Pasadena, CA. His current research interests are in the development of materials and processes for MEMS using electrochemical techniques, such as electrodeposition and electrochemical micromachining.

Jeffrey K. Yee received his BS degree in electrical engineering from the University of California, Berkeley in 1999. He has worked as a processing engineer at Advanced Microdevices, Sunnyvale, CA, as well as a mathematics tutor/teacher within the Oakland School District, CA. He is currently pursuing his MS/PhD in electrical engineering from the University of California, Los Angeles, focusing on MEMS magnetic sensors.

Deok-Yong Park received his BS degree (1986) in metallurgy and materials engineering, and MS degree (1988) in materials engineering from the Hanyang University, Republic of Korea. In 2000, he obtained his PhD degree in materials science and engineering from the University of California, Los Angeles. From 1988 to 1995, he worked at the Research and Development Center of LG Metals Corp., Republic of Korea as a senior research engineer. He is currently a post-doctor researcher working on the development of magnetic thin films using electrodeposition process for MEMS applications in the Chemical Engineering Department, University of California, Los Angeles.

Bong-Young Yoo is currently pursuing his PhD degree in materials science and engineering at University of California, Los Angeles. He received the MS in metallurgical engineering from the Yonsei University, Seoul, Republic of Korea in 1992. He worked as a processing engineer at Semiconductor R&D Center of Samsung electronics at Kiheung, Republic of Korea, from 1994 to 1999. He is currently focusing on the development of electrodeposited magnetic thin films.

Morton Schwartz received his BA and MA in chemistry from Indiana University in 1942. He had to take leave from his doctoral studies to join the war effort. He has over 40 years of industrial experience in the areas of electrodeposition and metal finishing. He was technical director of Surface Alloys Engineering Corp. (1948–1956), Kelite Chemicals Corp. (1956–1969), Electrochemical Division of Plessey (1971–1973), and vice president of Microplate Co. (1969–1971). He has been an electrochemical/metal finishing consultant since 1974, and a visiting scholar and then a visiting research engineer at the University of California, Los Angeles, since 1985. He has been an instructor/lecturer for numerous short courses on deposition technology, electroplating and metal finishing for UCLA Extension, AESF, and the Continuing Education Institute—USA/Europe. He received the Millhorn Award of the LA Branch, AESF (1973), Metal Finishers Association of Southern California "Man-of-the-Year Award" (1975) and the AESF's Leadership (proctor) and Past Presidents (1993) Awards. He is an honorary member of AESF, and emeritus member of the Electrochemical Society and the American Society for Metals.

Ken Nobe received his BS degree in chemistry and chemical engineering from the University of California, Berkeley and his PhD degree in engineering (with fields of study in chemical physics, mass transfer, and thermodynamics) from the University of California, Los Angeles. His industrial experience includes research on high polymer materials (polyacetylene) at Air Reduction Research Laboratories in Murray Hill, NJ and kinetics of high temperature reactions at Ramo-Wooldridge Corp. in El Segundo, CA. He was the chairman of the Department of Chemical, Nuclear and Thermal Engineering (1978–1983) and founding chairman of the Department of Chemical Engineering from 1983 to 1984. At the University of California, Los Angeles, he teaches courses in chemical engineering, phenomenological and statistical thermodynamics, electrochemistry and corrosion. His current research interests are in electro-organic synthesis, biochemistry, high rate electrodissolution processes, corrosion, and electrodeposition.

Jack W. Judy received the PhD and MS degrees from the University of California, Berkeley, CA in 1996 and 1994 respectively, as well as the BSEE degree, with summa cum laude honors, from the University of Minnesota, Minneapolis, MN in 1989. He has been on the faculty of the Electrical Engineering Department at the University of California, Los Angeles since 1997, where he is currently an assistant professor. He has also worked for Silicon Light Machines, Sunnyvale, CA, an optical-MEMS startup company, from 1996 to 1997. In his doctoral research, he developed a novel ferromagnetic microactuator technology that is useful for a variety of applications, including optical cross-connect switches. His present research interests include additional novel ferromagnetic MEMS, electronic noses, and neuroengineering projects, such as microprobes for Parkinson's disease research, electrode arrays for retinal prosthetics, wireless neural transceivers, and neural control systems for spinal cord injury, ocular motility, and deep brain stimulation.